# Radio Over Fiber Downlink Design for Spatial Modulation and Multi-Set Space-Time Shift-Keying

**YICHUAN LI, (Student Member, IEEE), IBRAHIM A. HEMADEH[ID], (Student Member, IEEE), MOHAMMED EL-HAJJAR, (Senior Member, IEEE), AND LAJOS HANZO[ID], (Fellow, IEEE)**

School of Electronics and Computer Science, University of Southampton, Southampton SO17 1BJ, U.K.

Corresponding author: Lajos Hanzo (lh@ecs.soton.ac.uk)

**ABSTRACT** Spatial modulation (SM) and multi-set space-time shift-keying (MS-STSK) are capable of striking a flexible design trade-off between the multiplexing and diversity gains attained. These techniques can also be combined with beamfoming for the sake of supporting reliable millimeter-wave (mmWave) communications. In this treatise, we propose an analogue radio-over-fiber (RoF) downlink network relying on SM and MS-STSK combined with beamforming and up-conversion to mmWave carrier frequencies, whilst using all-optical processing. In the proposed analogue RoF (A-RoF) system, most of the digital processing of the baseband SM and MS-STSK is carried out by the central unit and the implicitly carried bits of SM/MS-STSK, such as the antenna index selection and dispersion matrix selection bits, are recovered by the remote radio head of our A-RoF network for creating a multi-functional multiple-input multiple-output arrangement. As detailed by Hanzo *et al.*, the classic modulated bits are conveyed by the radio signal, without requiring any additional analogue-to-digital conversion and digital-to-analogue conversion before transmission from the antennas. Moreover, A-RoF-aided techniques are invoked for achieving optical processing-aided beamforming and optical up-conversion to an mmWave carrier frequency. Thus, we invoke A-RoF techniques for the generation of our SM/MS-STSK signal with the aid of optically up-converted millimetre-wave beamforming without using any electronic oscillators, mixers, or phase shifters. Furthermore, our A-RoF-aided system's bit error ratio performance is similar to the conventional all-electronic SM/MS-STSK scheme.

**INDEX TERMS** SM, MS-STSK, radio over fiber, beamforming, millimetre wave.

## NOMENCLATURE

| | |
|---|---|
| A-RoF | Analogue RoF |
| AC | Antenna Combination |
| ADC | Analogue-to-Digital Conversion |
| AoD | Angle of Departure |
| AWGN | Additive White Gaussian Noise |
| BER | Bit Error Ratio |
| BLAST | Bell Lab's Layer Space-Time |
| BPSK | Binary Phase Shift Keying |
| BS | Base-Station |
| C-RAN | Cloud Radio Access Network |
| CFBG | Chirped Fiber Bragg Grating |
| CU | Central Unit |
| DAC | Digital-to-Analogue |
| DAA | Demodulation and Antenna Arrangement |
| DSF | Dispersion-shifted Fiber |
| EBPF | Electronic Band Pass Filter |
| EDFA | Erbium-doped Fiber Amplifier |
| FBG | Fiber Bragg Grating |
| LD | Laser Diode |
| MIMO | Multiple-Input-Multiple-Output |
| ML | Maximum Likelihood |
| mmWave | Millimeter Wave |
| MS-STSK | Multi-set Space Time Shift Keying |
| MZM | Mach-Zehnder Modulator |
| OBPF | Optical Band Pass Filter |
| OC | Optical Circulator |
| ODSB | Optical Double Side-Band |

| O-E | Optical-to-electronic |
| OIL | Optical Interleaver |
| PD | Photo-detector |
| PRBS | Pseudorandom Binary Sequence |
| QAM/PSK | Quadrature Amplitude Modulation/ Phase Shift Keying |
| QPSK | Quadrature Phase Shift Keying |
| RF | Radio Frequency |
| RoF | Radio over Fiber |
| RRH | Remote Radio Head |
| SINR | Signal-to-Interference-plus-Noise Ratio |
| SM | Spatial Modulation |
| SNR | Signal-to-noise Ratio |
| STBC | Space Time Block Code |
| STSK | Space Time Shift Keying |
| TAA | Transmitter Antenna Arrays |

## LIST OF SYMBOLS

| $\hat{x}_1$ | Implicit bits |
| $\hat{x}_2$ | Classic modulated bits |
| $x_1$ | Implicit symbols |
| $x_2$ | Classic modulated symbols |
| $f_{RF}$ | RF frequency for radio carrier modulation |
| $f_{drive}$ | Drive frequency of MZM |
| $\lambda_n$ | Optical Wavelengths |
| $V_\pi$ | MZM switching voltage |
| $V_{dr}$ | MZM drive voltage |
| $\omega_{LO}$ | Angular center frequency of MZM drive signal |
| $\omega_{RF}$ | Angular center frequency of $f_{RF}$ |
| $J_n$ | The Bessel functions of the first kind and order n |
| $E_{in}$ | Input optical signal of MZM |
| $E_{MZM}$ | Output optical signal of MZM |
| $P_{laser}$ | LD's output power |
| $\omega_{oc}$ | Optical carrier's angular frequency |
| $N_t$ | Number of transmitter antennas |
| $N_r$ | Number of receiver antennas |
| $M$ | STSK space dimension |
| $Q$ | Number of dispersion matrix |
| $T$ | STSK time slots |
| $\mathcal{L}$ | PSK/QAM constellation size |
| $B_1$ | Antenna selection bits of MS-STSK |
| $B_2$ | Dispersion matrices selection bits of MS-STSK |
| $B_3$ | Classic modulated bits of MS-STSK |

## I. INTRODUCTION

As a result of the popularity of flawless multimedia services supported by the ubiquitous smartphones, cellular networks are approaching their capacity, especially in densely populated areas [2], [3]. Small cells are capable of overcoming the network capacity shortage with the aid of adding more cells of high-quality wireless coverage having a small cell radius [4]–[6]. Analogue Radio over Fiber (A-RoF) techniques are capable of supporting small cell deployment using centralized processing, where the small cell base-stations (BS) are connected using fiber [5] and only optical-to-electronic (O-E) conversion and RF amplification are
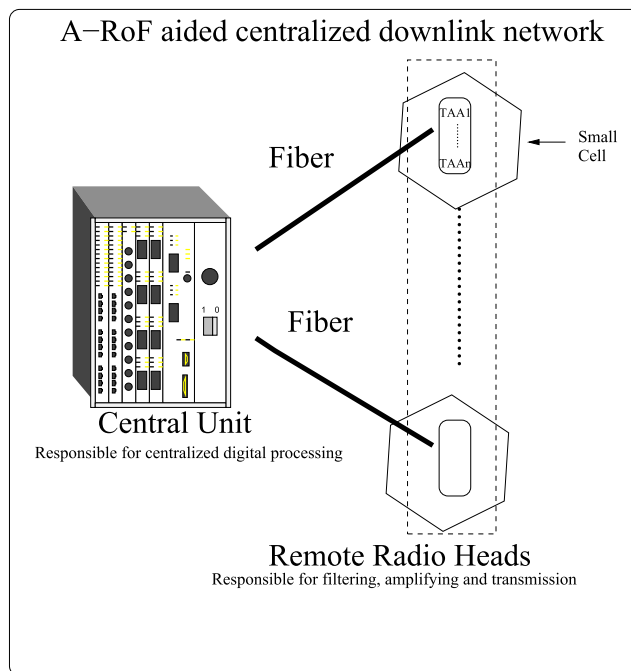


**FIGURE 1.** A-RoF aided centralized downlink network. The Central Unit performs centralized digital processing and radio modulation, while the Remote Radio Head carries out filtering, amplification and radio transmission.

required at the small-cell base station [7], [8]. A simplified schematic of the A-RoF-aided small cell system is shown in Figure 1, where a single central unit (CU) supports several remote small-cell radio heads. This architecture is potentially capable of reducing the overall cost of the network [7], [9]. As shown in Figure 1, the central unit is responsible for centralized digital processing, while the remote radio heads are used for radio transmission, including the O-E conversion, filtering, amplifications and then transmission from the transmitter antenna arrays (TAAs). This architecture is also applicapable to the popular cloud radio access networks (C-RAN) [10], [11], where a CU[1] carries out all the baseband signal processing [12], serving multiple low-complexity and low-cost remote radio heads (RRHs). The A-RoF transmissions [5], [13] to the RRHs invoked by C-RAN [9] are also capable of supporting the emerging small-cell technologies [9], [14].

Moreover, Millimeter Wave (mmWave) carries frequencies as naturally suitable for small cells owing to the associated short propagation range, thus reducing the inter-cell interference [2], [15]. However, traditional all-electronic mmWave processing requires high-frequency Radio Frequency (RF) mixers, which tend to degrade the link's performance [16]. We circumvent this problem with the aid of A-RoF techniques by dispensing with high frequency mixers and demonstrate that optical upconversion to mmWave frequencies are

---

[1]As suggested by one of the anonymous Reviewers, in the C-RAN literature the CU and baseband unit (BBU) terminologies are used interchangeably [9].

capable of outperforming its all-electronic counterpart [16], by exploiting the Mach-Zehnder Modulator's (MZM's) non-linearity, the fiber's non-linearity and the photo-detector's non-linearity for optical up-conversion [16]. Moreover, multi-frequency mmWave wavelength up-conversion techniques using four-wave mixing in a semiconductor optical amplifier has been proposed in [17] and [18], which aim for improving the capacity and for reducing the inter-channel interference. Additionally, photonic generation of multiple-frequency mmWave signals using tunable optical frequency combs has been presented in [19] for mitigating the crosstalk between the various optical network units involved. Furthermore, a combination of De-multiplexers and MZMs in a passive optical network [20] has been proposed for supporting the photonic generation of 60/120 GHz signals. By contrast, in this treatise we exploit the MZM's non-linearity combined with an Optical Interleaver (OIL) for optical upconversion and scalable beamforming.

On the other hand, as a key technique of reducing the inter-channel interference and of increasing the Signal-to-Interference-plus-Noise Ratio (SINR) of mmWaves, beamforming may be invoked to compensate for the short propagation range of mmWave communications and hence for achieving an SINR gain [21]. Furthermore, A-RoF aided beamforming relying on all-optical processing is capable of substantially reducing the complexity of our multi-functional Multiple-Input Multiple-Output (MF-MIMO) configuration, which is designed to combine the gains of spatial diversity, multiplexing and beamforming techniques, by avoiding the employment of phase shifters used in traditional electronic beamforming [13].

Let us now elaborate a little further on Spatial Modulation (SM) [22], which is a low-cost MIMO technique, where one out of $M$ transmit antennas is activated to transmit a single classic Quadrature Amplitude Modulation/Phase Shift Keying (QAM/PSK) symbol. Hence, in SM, in addition to the classic modulated bits, $log_2 M$ implicit antenna index based information bits are conveyed[2] [23]. SM is capable of striking a compelling trade-off between Bell Lab's Layered Space-Time (BLAST) and Alamouti's Space-Time Block Code (STBC), whilst relying on a reduced number of RF chains. Its further benefits are its ability to use a single-antenna based Maximum Likelihood (ML) detection scheme and the mitigation or elimination of inter-channel interference [24], [25]. Additionally, Space-Time-Shift-Keying (STSK) constitutes a generalization of SM, where one out of say $M$ number of dispersion matrices is activated for implicitly conveying $log_2 M$ bits, which can attain both diversity and multiplexing gains [25], [26]. Based on intrisincally amalgamating the philosophy of both SM and STSK, the concept of Multi-Set STSK (MS-STSK) was proposed in [27] as a further generalized architecture, which is capable of striking a beneficial design trade-off between the achievable multiplexing and diversity gains [27].

In A-RoF system's downlink, RF signals are transmitted over the optical fiber from the central unit to the remote radio head, where the centralized baseband processing is carried out. Then, the photo detected signal is transmitted by the antennas without the need for electronic processing in the baseband, such as modulation, DAC or ADC [5], [16]. In this paper, we propose a RoF system relying on centralized processing aided SM and MS-STSK combined with all-optical beamforming, while simultaneously achieving optical up-conversion to mmWave carrier frequencies.

In the proposed A-RoF network, the SM and MS-STSK information is modulated onto the two side-bands of an optically modulated signal in the central unit of Figure 1, which is up-converted from a frequency of 3 GHz to a mmWave frequency by pure optical processing utilising a MZM and an OIL. The side-band containing the implicit information[3] is decoded by the remote radio head of Figure 1. Furthermore, tunable optically aided beamforming can be achieved using optical Fiber Bragg Grating (FBG), which introduces a linear relationship between the time delays and the optical wavelengths by reflecting different wavelengths from different locations inside the FBG discussed in [21] and [28]. Moreover, the SM/MS-STSK signals are transmitted over a Dispersion-Shifted Fiber (DSF), which exibits a low dispersion in our proposed wavelength region [29]. This is used for mitigating the dispersion effects imposed on the optical fiber aided beamforming.

Thus, compared to a conventional cellular architecture, where the RF and baseband signal processing are integrated into a base station [9], our proposed design is capable of concentrating the digital baseband processing in the central unit. Hence the complexity of the remote radio head is reduced to that of low-cost filtering, switching and amplification [30] Against the above backdrop, the novel contributions of this paper are summarised as follows:

1) **Intelligent centralized-processing aided A-RoF network design**: We propose a sophisticated A-RoF network for supporting low-complexity SM or MS-STSK combined with all-optical beamforming and up-conversion to mmWave carrier frequencies. More explicitly, all-optical SM/MS-STSK processing is combined with beamforming in the mmWave spectral band. To the best of our knowledge, this is the first time that optical fiber aided analogue beamforming using CFBG is conceived for mmWave communications.

2) **Optical processing aided SM/MS-STSK encoding scheme**: We propose an architecture for carrying both implicit antenna-index-based information and classically modulated information by SM/MS-STSK intrinsically amalgamated with optical processing. Again, this avoids the ADC and RF carrier modulation at the remote radio head. Instead, an optically up-converted

---

[2] We refer to the antenna selection index in SM as the implicit information.

[3] In MS-STSK, the implicit information refers to the antenna selection index and dispersion matrix index information.

mmWave signal carries the SM and MS-STSK symbols, which are then fed into linear uniform arrays for beamforming, hence requiring no additional electronic signal processing at the remote radio heads.

The rest of the paper is organised as follows. Section II presents the A-RoF aided SM encoding network, where the conventional electronic SM scheme and the proposed model are presented and discussed. Then, in Section III, the A-RoF aided MS-STSK scheme is introduced and analyzed, followed by our conclusions in Section IV.

## II. A-RoF NETWORK DESIGN FOR SM

In this paper, we propose an all-optical processing aided Multi-Functional MIMO (MF-MIMO) [31] system, where SM/MS-STSK, optical upconversion and optical fiber aided beamforming were amalgamated. In A-RoF networks, most of the digital processing is carried out in the central unit of Figure 1. In this contribution, we propose a novel A-RoF network carrying SM symbols, which can be used both for the mobile fronthaul or backhual.

In the proposed network, after the conventional electronic SM encoding, the SM information is transmitted over the dispersion-shifted fiber, where the signal is up-converted to a mmWave carrier frequency and linearly time-delayed signals are attained with the aid of FBGs for achieving an angularly selective beamforming effect. In this section, we first present the conventional SM electronic encoding design and then we discuss the proposed system architecture and its performance.
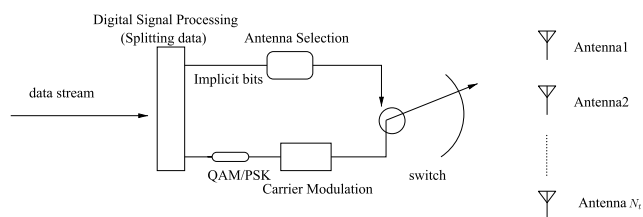


**FIGURE 2.** Conventional electronic SM encoding scheme used by the Base Stations of the conventional cellular architecture.

### A. CONVENTIONAL ELECTRONIC SM ENCODING SCHEME

Figure 2 shows the conventional SM encoding process using $N_t$ transmit antennas, where the input bits are partitioned into two streams. The first stream is used for activating one out of the $N_t$ transmit antennas, while the second stream is used for modulating a classical QAM/PSK symbol,[4] as shown in Figure 2. Hence, the transmitted symbol implicitly carries the selected antenna index information.

In the traditional architecture, SM encoding is carried out at each BS, adding extra cost and complexity to the small-cell system [9]. By contrast, in our proposed design, the digital processing is concentrated to the central unit, as detailed in the following sections. To elaborate a little further, our proposed A-RoF-aided SM design is capable of confining

the SM encoding to a single central unit, hence substantially easing the burden imposed on small-cell base stations.

### B. PROPOSED A-RoF-AIDED SM DESIGN

Upon introducing optical fiber aided beamforming and optical up-conversion, our system transmits the SM symbols using a mmWave carrier and all-optical processing, relying on the remote radio heads of Figure 1. Figure 3 and 4 highlight the operation of our A-RoF aided SM system and the corresponding spectral-domain manipulations. In the following, we will detail the signal processing in our system of Figure 3, while referring to the corresponding spectral-domain manipulations seen in Figure 4.[5]

### 1) SM ENCODING

Similar to the conventional electronic SM encoding scheme, a pseudorandom binary sequence (PBRS) is generated and split into two streams that convey the antenna selection bits $\hat{x}_1$ as well as the classic modulated bits $\hat{x}_2$. Then, as shown in Figure 3, we map the implicit antenna-index bits to a $2^L - QAM/PSK$ scheme, where $2^L$ represents the number of transmitter antenna elements of each antenna array of Figure 3. Similarly, the classic modulated bits are conveyed by $2^M - QAM/PSK$ symbols according to the system requirements. Note in the interest of explicit clarity that in contrast to the conventional electronic SM encoding scheme, in our amalgamated optical/RF system both SM streams are conveyed by QAM/PSK symbols over the fiber. This ensures that they have the same symbol rate during their transmission in the A-RoF link. For example, if a PRBS block of the bits $b_1 \ldots b_3$ is transmitted, $b_1, b_2$ are used for the implicit antenna-index bits as $\hat{x}_1$ for activating one out of four antenna elements, while $b_3$ is used for classic Binary Phase Shift Keying (BPSK) modulated bits for optical transmission as $\hat{x}_2$. To ensure that $b_3$ is conveyed by the $b_1, b_2$-based antenna element after the A-RoF link, $b_1, b_2$ are conveyed by a Quadrature Phase Shift Keying (QPSK) symbol.

Afterwards, both types of SM symbols are carried by a RF frequency of $f_{RF}$ and fed into a pair of LDs for direct modulation, as shown in Figure 3. The two LDs are directly modulated by $x_1$ and $x_2$ to generate a pair of wideband signals, respectively, as shown at ① and ② of Figure 4. Then, the left side-band of ① carrying $x_1$ and the right side-band of ② carrying $x_2$ are retained by the Optical Band Pass Filters (OBPFs) and combined to a new ODSB signal using an optical combiner, as shown in Figure 3 and marked by ③ of Figure 4.

Thus, SM encoding relies on Optical Double Side-band (ODSB) modulation associated with an RF frequency of $f_{RF}$, where both the implicit symbols $x_1$ used for antenna selection and the classic modulated symbols $x_2$ are mapped to one of the side-bands, each using a combination of Laser Diodes (LDs) and OBPFs.

---

[4]In our paper, we term data symbol for transmission as classic modulated symbol.

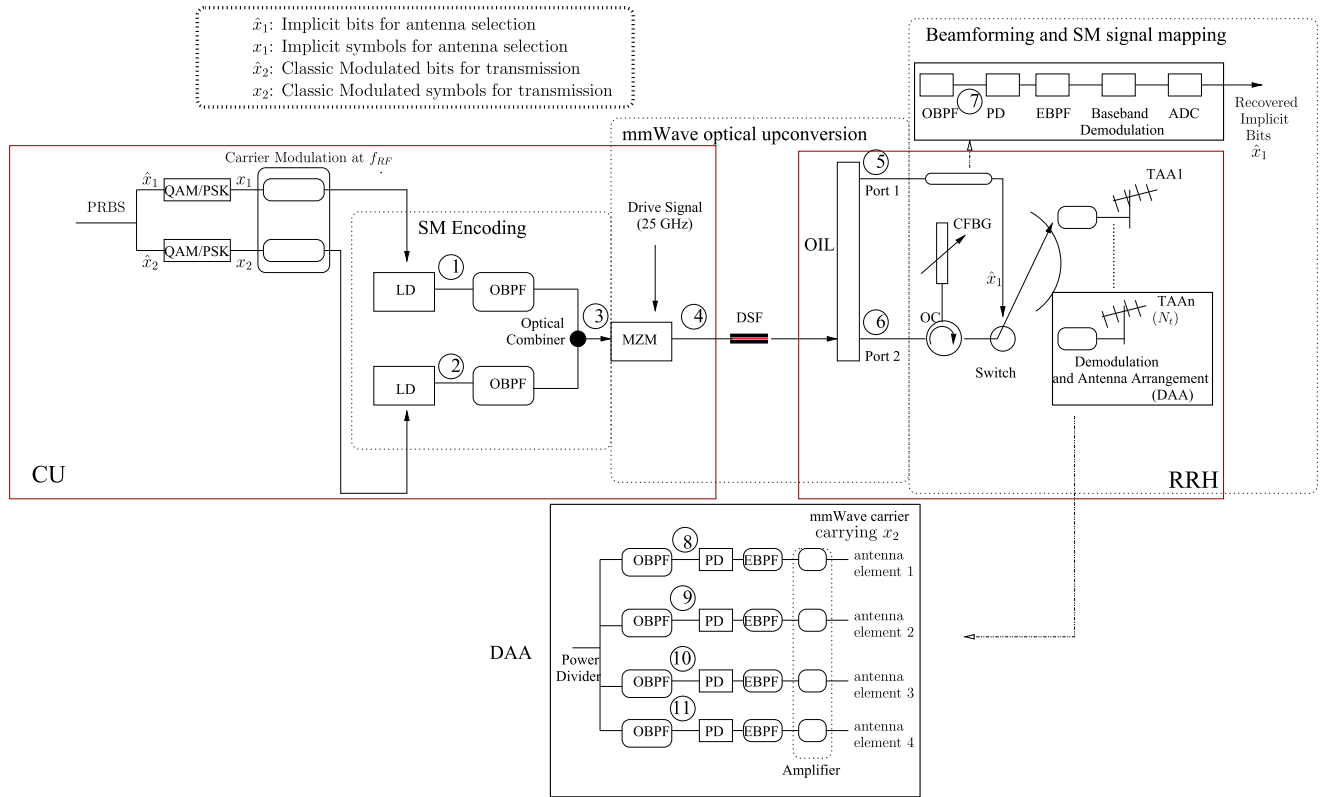[5]The circled numbers of Figure 3 correspond to the numbers in Figure 4

**FIGURE 3.** A centralized A-RoF aided SM encoding scheme. The CU performs digital modulation, carrier modulation, E-O conversion and SM encoding, while the RRH implements the radio functions (filtering, O-E conversion, photo-detection, amplifying and radio transmission), as well as SM implicit data recovery and SM switching.

### 2) mmWAVE OPTICAL UPCONVERSION

Afterwards, optical modulation is employed using the Mach-Zenhder Modulator (MZM) of Figure 3, where, as demonstrated at ④ of Figure 4, the drive voltage of the MZM can be appropriately tuned in order to copy the ODSB signal carrying $x_1$ and $x_2$ to multiple wavelengths. This will result in multi-wavelength signals that can be transmitted over mmWaves, by beneficially exploiting the MZM's non-linearity[6] [13]. Then, the multi-wavelength ODSB signal is transmitted over a DSF at the zero-dispersion wavelength in the vicinity of 1550 nm [29], for the sake of mitigating the dispersion effects, whilst aiming for a constant time-delay. As shown in Figure 3, optical up-conversion is applied using an optical interleaver, as illustrated in Figure 5. The multi-wavelength signal at the fiber's output is fed into the OIL, where the two outputs of Figure 5 provide the beat frequencies representing the mmWave frequency carrying $x_2$ and the RF frequency $f_{RF}$ carrying $x_1$, respectively. For example, if a multi-wavelenth signal of the ODSBs having the center frequencies of $\lambda_1$, $\lambda_2$ and $\lambda_3$, shown in Figure 5 is fed into the OIL, Port 1 of the OIL retains the optical carrier and the left side-band of $\lambda_2$ as well as the right side-bands

of $\lambda_1$ and $\lambda_3$ while Port 2 outputs the remaining spectrum. The OIL acts as a periodic filter, which splits the spectrum for generating a set of appropriately beating frequencies after the PDs of the 'Beamforming and SM signal mapping' block of Figure 3, generating the RF and mmWave frequencies in our proposed system. Generally, Port 1 retains the optical carrier and the left side-bands of $\lambda_{2n}$ as well as the right side-bands of $\lambda_{2n-1}$, while Port 2 outputs the right side-bands of $\lambda_{2n}$ as well as the optical carrier and the left side-bands of $\lambda_{2n-1}$. The corresponding spectra of Port 1 and Port 2 are shown at ⑤ and ⑥ of Figure 4.

### 3) BEAMFORMING AND SM SIGNAL MAPPING

Following the OIL, the antenna selection bits $\hat{x}_1$ are recovered after passing the signal gleaned at Port 1 of Figure 3 through the OBPF, Photo Detection (PD), Electronic Band Pass Filter (EBPF), baseband demodulation and the ADC components, where the OBPF retains the spectrum of ⑦ of Figure 4, the PD achieves the O-E conversion, the EBPF obtains the $f_{RF}$ RF signal and the ADC converts the analogue RF signal to digital symbols for SM switching. The photo-detected RF signal used for antenna selection appears at $f_{RF}$. On the other hand, the output of Port 2 is fed into a tunable chirped FBG, which imposes a linear time delay on each wavelength by reflecting different wavelength from different locations.
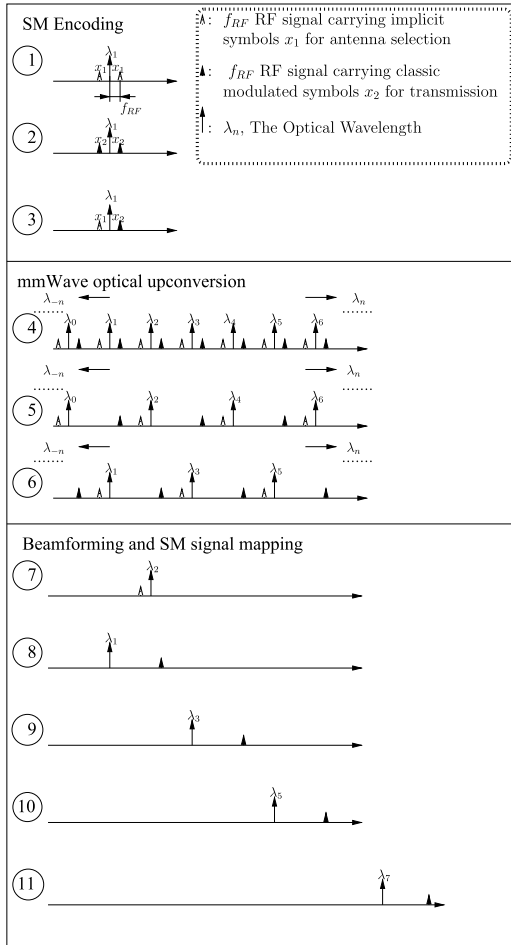
---

[6]In Figure 4, we portrayed the comb-like signals for the sake of showing the spectral evolution in our system design in a stylized format. In fact, the amplitude of the corresponding wavelengths relies on both the harmonics' order and on the switching voltage as well as on the amplitude of the MZM's drive voltage, which will be analyzed in Section II-B.3.a

**FIGURE 4.** Spectral-domain charaterization of proposed system of Figure 3.



**FIGURE 5.** An optical interleaver.

of port 1 and port 2 of Figure 3, where the corresponding frequencies will be processed in order to form stages ⑦, ⑧, ⑨, ⑩ and ⑪ of Figure 4. The photo-detected RF signal after stage ⑦ is used for antenna selection, while those of ⑧, ⑨, ⑩ and ⑪ are used for mmWave signal generation. The details of these spectral shaping operations will be discussed in the following sections.

In contrast to the conventional SM encoding scheme of Figure 2, our proposed system is capable of carrying the SM symbols encapsulated in a multi-wavelength optical signal over the optical fiber. At the fiber's output, the implicit antenna index bits are recovered, while the corresponding classic modulated symbols are modulated by a up-converted mmWave signal. Our design eliminates the need for both the ADC and the DAC at the remote radio head, which substantially reduces the cost and complexity of the remote radio head. The optically up-converted and beamformed mmWave signal can be directly fed into the TAA, without any additional electronic processing for modulation and demodulation, where the electronic filters and amplifiers are used for ensuring that the amplitudes of the mmWave signals emitted from each TAA element are appropriately adjusted. In the following, we detail both the rationale and mathematical model of our system regarding mmWave generation and beamforming.

*a: mmWAVE GENERATION*

As presented in the middle dashed box of Figure 3, the MZM and OILs contribute to the mmWave signal generation. The harmonics generated by the MZM's nonlinearity result in multiple wavelengths, where each wavelength carries a copy of the ODSB signal of ③ of Figure 4.[7] Assuming that $E_{in}$ is the ODSB input of the MZM, as detailed in [32], higher-order optical side-bands are generated relying on the voltage of the drive signal imposed on the MZM. The resultant optical signal is given by:

$$E_{MZM}(t)$$
$$= cos[\pm\frac{\pi}{4} + \frac{\pi V_{dr}cos(\omega_{LO})}{2V_{\pi}}]E_{in}(t)$$
$$= \frac{E_{in}(t)}{\sqrt{2}}[J_0(\frac{\pi|V_{dr}|}{2V_{\pi}}) + 2\sum_{n=1}^{\infty}(-1)^n J_{2n}(\frac{\pi V_{dr}}{2V_{\pi}})cos(2n\omega_{LO}t)$$
$$\pm 2\sum_{n=1}^{\infty}(-1)^n J_{2n-1}(\frac{\pi V_{dr}}{2V_{\pi}})cos((2n-1)\omega_{LO}t)], \quad (1)$$

[7]$\lambda_1$ of Figure 4 is the LD's optical carrier

The time-delayed multi-wavelength signal carrying $x_2$ is then transmitted by the activated antenna, where the photo-detectors of the Demodulation and Antenna Arrangement (DAA) block of Figure 3 receive the corresponding time-delayed wavelengths and then convert them to a mmWave signal having a frequency of $(f_{RF} + f_{drive})$. Therefore, the mmWave signals of the DAA associated with the linear time delays are passed on to the corresponding Transmitter Antenna Array (TAA), whose index has been decoded after the photo detection stage of Figure 3.

More specifically, as shown in Figure 4, the spectra at ① and ② represent the directly modulated ODSB optical signals of the LDs of Figure 3, where $x_1$ and $x_2$ are mapped to the side-bands having a center frequency of $f_{RF}$. Then, following the appropriate filtering by the OBPF after each LD of Figure 3, we obtain a new ODSB, with $x_1$ being mapped to the left and $x_2$ to the right side-band, as shown at ③ of Figure 4. The ODSB signal is then converted to a multi-wavelength signal by beneficially exploiting the MZM's non-linearity of Figure 3, resulting in the spectra at ④ of Figure 4. The OIL of Figure 3 is then used for appropriately filtering the spectrum to be utilised for mmWave generation and antenna-index bit recovery. The stages ⑤ and ⑥ show the spectrum
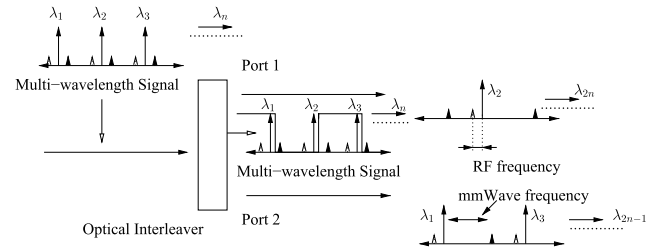
where the $E_{MZM}$ is the output field of the MZM with a switching voltage of $V_\pi$, which induces a phase-shift of $\pi$ for each arm, while $V_{dr}$ is the drive voltage of the angular center frequency of $\omega_{LO}/(2\pi)$. Here, $J_n(\frac{\pi V_{dr}}{2V_\pi})$ is the Bessel function of the first kind and order $n$, which determines both the number and the amplitude of the side-bands.

The resultant multi-wavelength ODSB signal carrying the RF of $\omega_{RF}$ is then fed into the OIL of Figure 3, after transmission over the optical fiber, where the OIL removes some of the multi-wavelength signal frequencies. Explicitly, in the case of Port 2 of the OIL of Figure 3, $\lambda_1$ associated with the left side-band, $\lambda_3$ with the right side-band as well as the right side band of $\lambda_2$ and $\lambda_4$ are filtered out, as shown at ⑤ of Figure 4. In this case, the beat frequency between $\lambda_1$ and the right side-band of $\lambda_3$ is photo-detected, which generates a frequency of $\omega_{RF} + \omega_{LO}$, namely 28 GHz in our design and completes the mmWave frequency generation. The up-converted frequency relies on the frequency $\omega_{rf}$ of the drive voltage imposed on the MZM of Figure 3, which can be appropriately tuned in order to up-convert the signal to any desired frequency in the mmWave spectrum.

More specifically, if a RF signal of center frequency of 3 GHz is directly modulated by the LDs of Figure 3, a multi-wavelength ODSB signal carrying a 3 GHz RF signal is then generated with the aid of a MZM's drive signal of 25 GHz, resulting in a wavelength spacing of 25 GHz among the neighbouring $\lambda_n$ components. Then, as shown in stages ④, ⑤ and ⑥ of Figure 4, the OIL of Figure 3 removes some of the frequencies output by Port 1 and Port 2 of the OIL. Thus, on one hand, the output signal of Port 1 is filtered by the OBPF seen at ⑦ of Figure 3. Then, after processing by the Beamforming and SM signal mapping block of Figure 3, the beat frequency becomes 3 GHz, which is used for the implicit bits recovery of SM. On the other hand, following the transmission of the output signal of Port 2 of the OIL in the CFBG scheme of Figure 3 for beamforming, the signal is fed into the DAA of Figure 3, resulting in the time-delayed signals of stages ⑧, ⑨, ⑩ and ⑪ of Figure 3. After the PD, the beat frequency obtained is the up-converted mmWave frequency of 28 GHz. The beamforming scheme will be further detailed in the next section.

*b: BEAMFORMING*

Due to the short mmWave propagation range, we exploit our optical signal processing aided beamforming scheme to extend the propagation range of mmWave communications. In our design, beamforming is introduced by exploiting the constant time-delay difference between the neighbouring antenna elements of each transmitter, where the constant time delay difference is obtained with the aid of CFBG, which impose different time-delays on different wavelengths due to their different locations of reflection [28]. Furthermore, CFBG supports true-time delay based beamforming for wideband signals, which is achieved by avoiding the beam-squinting introduced by the popular phase shifting based beamforming scheme [21].

The signal generated at the output of the OIL of Figure 3 is transmitted to an optical circulator (OC), which is a three-port component, where the time-delayed multi-wavelength signals reflected by CFBG are forwarded to one of the DAA block of Figure 3. The time delay introduced by CFBG is linearly proportional to the transmitting wavelengths, which can be translated to a specific beamsteering direction [33]. Furthermore, the reflected frequency spectrum of the CFBG can be appropriately tuned to control the time delay, thus adjusting the beamsteering direction [34]. Subsequently, the output of the OC is split into several branches shown in the DAA block of Figure 3. As shown at ⑧, ⑨, ⑩, ⑪ of Figure 4, the desired wavelength is retained with the aid of optical BPF in DAA of Figure 3. Thus, each branch outputs the carrier associated with the same symbol but different delays. After the PD and electronic BPF of the DAA of Figure 3, the delayed carriers are fed into the antenna array elements, which can be translated into different beamforming patterns according to the appropriately tuned time delay differences. We will demonstrate that our system is capable of both mmWave carrier generation and beamforming with aid of the CFBG-induced time-delay as detailed mathematically in the following section.

## C. MATHEMATICAL MODEL OF MULTI-WAVELENGTH SIGNAL BEAMFORMING

Since the time-delay imposed by the CFBG is applied in the optical domain, there may be a delay-difference between the modulated optical signal and its corresponding photo-detected beat signal. In this section, we show mathematically that the time-delay differences between the photo-detected RF signals of the neighbouring antennas remain constant. As mentioned in Section II-B, the RF signal is directly modulated by LDs and the input optical field of the MZM of Figure 3 is formulated as:

$$E_{in}(t) = \sqrt{P_{Laser}} e^{j\omega_{oc}t}[1 + cos(\omega_{RF}t)], \quad (2)$$

where $P_{Laser}$ is the LD's output power and $\omega_{oc}$ denotes the optical carrier's angular frequency corresponding to $\lambda_1$ of Figure 4. The MZM output field expressed in Equation (1) can be combined with Equation (2) to arrive at:

$$
\begin{aligned}
&E_{MZM}(t) \\
&= cos(\pm\frac{\pi}{4} + \frac{\pi V_{dr} cos(\omega_{LO})}{2V_\pi})E_{in}(t) \\
&= \frac{\sqrt{P_{laser}}[1 + cos(\omega_{RF}t)]e^{j\omega_{oc}t}}{\sqrt{2}}[J_0(\frac{\pi|V_{dr}|}{2V_\pi}) \\
&\quad + 2\sum_{n=1}^{\infty}(-1)^n J_{2n}(\frac{\pi V_{dr}}{2V_\pi})cos(2n\omega_{LO}t) \\
&\quad \pm 2\sum_{n=1}^{\infty}(-1)^n J_{2n-1}(\frac{\pi V_{dr}}{2V_\pi})cos((2n-1)\omega_{LO}t)] \\
&= \frac{\sqrt{P_{laser}}e^{j\omega_{oc}t}}{\sqrt{2}}[J_0(\frac{\pi|V_{dr}|}{2V_\pi})[1 + cos(\omega_{RF}t)]
\end{aligned}
$$

$$+ 2 \sum_{n=1}^{\infty} (-1)^n J_{2n}(\frac{\pi V_{dr}}{2V_{\pi}})[cos(2n\omega_{LO}t)$$

$$+ \frac{cos((2n\omega_{LO}+\omega_{RF})t)+cos((2n\omega_{LO}-\omega_{RF})t)}{2}]$$

$$\pm 2 \sum_{n=1}^{\infty} (-1)^n J_{2n-1}(\frac{\pi V_{dr}}{2V_{\pi}})[cos((2n-1)\omega_{LO}t)$$

$$+ \frac{cos(((2n-1)\omega_{LO}+\omega_{RF})t)+cos(((2n-1)\omega_{LO}-\omega_{RF})t)}{2}]$$

$$= \frac{\sqrt{P_{laser}}}{\sqrt{2}}[J_0(\frac{\pi |V_{dr}|}{2V_{\pi}})[e^{j\omega_{oc}t} + e^{j(\omega_{oc}+\omega_{RF})t}/2$$

$$+ e^{j(\omega_{oc}t-\omega_{RF}t)}/2] + 2 \sum_{n=1}^{\infty} (-1)^n J_{2n}(\frac{\pi V_{dr}}{2V_{\pi}})$$

$$\times [e^{j(\omega_{oc}+2n\omega_{LO})t}/2 + e^{j(\omega_{oc}-2n\omega_{LO})t}/2$$

$$+ \frac{e^{j(\omega_{oc}+2n\omega_{LO}+\omega_{RF})t}/2 + e^{j(\omega_{oc}-2n\omega_{LO}-\omega_{RF})t}/2}{2}$$

$$+ \frac{e^{j(\omega_{oc}+2n\omega_{LO}-\omega_{RF})t}/2 + e^{j(\omega_{oc}-2n\omega_{LO}+\omega_{RF})t}/2}{2}]$$

$$\pm 2 \sum_{n=1}^{\infty} (-1)^n J_{2n-1}(\frac{\pi V_{dr}}{2V_{\pi}})$$

$$\times [\frac{e^{j(\omega_{oc}+(2n-1)\omega_{LO})t} + e^{j(\omega_{oc}-(2n-1)\omega_{LO})t}}{2}$$

$$+ \frac{e^{j(\omega_{oc}+(2n-1)\omega_{LO}+\omega_{RF})t}/2 + e^{j(\omega_{oc}-(2n-1)\omega_{LO}-\omega_{RF})t}/2}{2}$$

$$+ \frac{e^{j(\omega_{oc}+(2n-1)\omega_{LO}-\omega_{RF})t}/2 + e^{j(\omega_{oc}-(2n-1)\omega_{LO}+\omega_{RF})t}/2}{2}]. \tag{3}$$

Thus, after the OIL and the DAA block of Figure 3, we arrive at multiple mmWave signals of the same frequency but having different time-delays. Here, the signal at the output of Port 2 after the OIL block of Figure 3 can be expressed from Equation (4) as follows:

$$E_{IL_{bottom}}(t)$$

$$= \frac{\sqrt{P_{laser}}}{\sqrt{2}}[J_0(\frac{\pi |V_{dr}|}{2V_{\pi}})(\frac{e^{j(\omega_{oc}-\omega_{RF})t}}{2} + e^{j\omega_{oc}t})$$

$$+ 2 \sum_{n=1}^{\infty} (-1)^n J_{2n}(\frac{\pi V_{dr}}{2V_{\pi}})$$

$$\times (\frac{e^{j(\omega_{oc}-2n\omega_{LO}-\omega_{RF})t} + e^{j(\omega_{oc}+2n\omega_{LO}-\omega_{RF})t}}{4}$$

$$+ \frac{e^{j(\omega_{oc}+2n\omega_{LO})t} + e^{j(\omega_{oc}-2n\omega_{LO})t}}{2})$$

$$\pm 2 \sum_{n=1}^{\infty} (-1)^n J_{2n-1}(\frac{\pi V_{dr}}{2V_{\pi}})$$

$$\times \frac{e^{j(\omega_{oc}-(2n-1)\omega_{LO}+\omega_{RF})t} + e^{j(\omega_{oc}+(2n-1)\omega_{LO}+\omega_{RF})t}}{4}]. \tag{4}$$

After the OIL, the beat frequency can be obtained by the DAA block seen at the bottom of Figure 3, where the right

side-band of even wavelength ($\lambda_2$ and $\lambda_4 \ldots$) and its neighbouring wavelengths' optical carrier ($\lambda_1$ and $\lambda_3 \ldots$) are retained and mapped to each line of the DAA block, as shown in Figure 4. Thus, assuming that no time-delay scheme is applied, the resultant photo-detected signal of the top line of the DAA block of Figure 3 is given as follows:

$$E_{PD}(t)$$

$$\propto |E_{IL}(t)|^2$$

$$= |\frac{\sqrt{P_{laser}}}{\sqrt{2}}[J_0(\frac{\pi |V_{dr}|}{2V_{\pi}})\frac{e^{j\omega_{oc}t}}{2} \mp 2J_1(\frac{\pi V_{dr}}{2V_{\pi}})$$

$$\times \frac{e^{j(\omega_{oc}+\omega_{LO}+\omega_{RF})t}}{2}]|^2$$

$$= \frac{P_{laser}}{8}[J_0^2(\frac{\pi |V_{dr}|}{2V_{\pi}}) + 4J_1^2(\frac{\pi V_{dr}}{2V_{\pi}}) \mp 4J_0(\frac{\pi V_{dr}}{2V_{\pi}})J_1(\frac{\pi V_{dr}}{2V_{\pi}})$$

$$\times cos(\omega_{LO}+\omega_{RF})t]. \tag{5}$$

In order to achieve the desired beamforming effect, having an identical time-delay difference between neighbouring wavelengths is required. Thus, in terms of the first line of DAA shown in Figure 3, which feed the signal to antenna element 1 of each TAA, the CFBG applies the time-delay $t_1$ to the optical carrier $\lambda_1$ and $t_2$ to $\lambda_2$'s right side-band $x_2$ upon introducing $\Delta t = t_2 - t_1$. The corresponding photo-detected beat signal is expressed as follows:

$$E_{PD_{delayed}}(t)$$

$$\propto |E_{IL_{delayed}}(t)|^2$$

$$= |\frac{\sqrt{P_{laser}}}{\sqrt{2}}[J_0(\frac{\pi |V_{dr}|}{2V_{\pi}})\frac{e^{j\omega_{oc}(t-t_1)}}{2} \mp 2J_1(\frac{\pi V_{dr}}{2V_{\pi}})$$

$$\times \frac{e^{j(\omega_{oc}+\omega_{LO}+\omega_{RF})(t-t_2)}}{2}]|^2$$

$$= \frac{P_{laser}}{8}[J_0^2(\frac{\pi |V_{dr}|}{2V_{\pi}}) + 4J_1^2(\frac{\pi V_{dr}}{2V_{\pi}}) \mp 4J_0(\frac{\pi V_{dr}}{2V_{\pi}})J_1(\frac{\pi V_{dr}}{2V_{\pi}})$$

$$\times cos((\omega_{LO}+\omega_{RF})(t - t_2) + \omega_{oc}(t_1 - t_2))]$$

$$= \frac{P_{laser}}{8}[J_0^2(\frac{\pi |V_{dr}|}{2V_{\pi}}) + 4J_1^2(\frac{\pi V_{dr}}{2V_{\pi}}) \mp 4J_0(\frac{\pi V_{dr}}{2V_{\pi}})J_1(\frac{\pi V_{dr}}{2V_{\pi}})$$

$$\times cos((\omega_{LO}+\omega_{RF})(t - t_2 - \frac{\omega_{oc}\Delta t}{\omega_{LO}+\omega_{RF}}))]. \tag{6}$$

Similarly, assuming that the delay $t_3$ is applied to the optical carrier $\lambda_3$ of ⑥ of Figure 4 , while $t_4$ to the right side-band of $\lambda_4$ and that $\Delta t = t_2 - t_1 = t_4 - t_3$, the photo-detected signal of the second line of DAA block of Figure 3, which is fed into the antenna element 2 of each TAA of Figure 3 becomes:

$$E_{PD_{delayed_2}}(t)$$

$$\propto |\frac{\sqrt{P_{laser}}}{\sqrt{2}}[-2J_2(\frac{\pi V_{dr}}{2V_{\pi}})\frac{e^{j(\omega_{oc}+2\omega_{LO})(t-t_3)}}{2} \pm 2J_3(\frac{\pi V_{dr}}{2V_{\pi}})$$

$$\times \frac{e^{j(\omega_{oc}+3\omega_{LO}+\omega_{RF})(t-t_4)}}{2}]|^2$$

$$= \frac{P_{laser}}{8}[4J_2^2(\frac{\pi |V_{dr}|}{2V_{\pi}})+4J_3^2(\frac{\pi V_{dr}}{2V_{\pi}}) \mp 8J_2(\frac{\pi V_{dr}}{2V_{\pi}})J_3(\frac{\pi V_{dr}}{2V_{\pi}})$$

$$\times cos((\omega_{LO}+\omega_{RF})(t - t_4) + (\omega_{oc}+2\omega_{LO})(t_3 - t_4))]$$

$$= \frac{P_{laser}}{8}[4J_2^2(\frac{\pi|V_{dr}|}{2V_\pi})+4J_3^2(\frac{\pi V_{dr}}{2V_\pi}) \mp 8J_2(\frac{\pi V_{dr}}{2V_\pi})J_3(\frac{\pi V_{dr}}{2V_\pi})$$

$$\times cos((\omega_{LO}+\omega_{RF})(t-t_4-\frac{(\omega_{oc}+2\omega_{LO})\Delta t}{\omega_{LO}+\omega_{RF}}))]. \quad (7)$$

Thus, following the same philosophy, the photo-detected signal of third line of DAA of Figure 3 is,

$$E_{PD_{delayed_3}}(t)$$

$$\propto \frac{P_{laser}}{8}[4J_4^2(\frac{\pi|V_{dr}|}{2V_\pi})+4J_5^2(\frac{\pi V_{dr}}{2V_\pi}) \mp 8J_4(\frac{\pi V_{dr}}{2V_\pi})J_5(\frac{\pi V_{dr}}{2V_\pi})$$

$$\times cos((\omega_{LO}+\omega_{RF})(t-t_6-\frac{(\omega_{oc}+4\omega_{LO})\Delta t}{\omega_{LO}+\omega_{RF}}))], \quad (8)$$

where the delay $t_5$ is applied to the optical carrier $\lambda_5$ of ⑥ of Figure 4, while $t_6$ is applied to the right side-band of $\lambda_6$ and $\Delta t = t_2 - t_1 = t_4 - t_3 = t_6 - t_5$.

By comparing Equations (6), (7) and (8), it becomes clear that there exists some delay between each photo-detected output signal and for antenna element of each DAA, the delay will not be exactly the same. However, the time delay difference of the photo-detected signals fed into neighbouring antenna elements of the DAA block of Figure 3 will be constant. Specifically, due to the linear relationship between the time-delay and the wavelengths, we obtain $\Delta t = t_2-t_1 = t_4 - t_3 = t_6 - t_5$ and $t_2 - t_4 = t_4 - t_6$. The time-delay difference of the output signals between antenna element 1 and antenna element 2 of the DAA block of Figure 3 is $(t_4 - t_2) + \frac{2\omega_{LO}\Delta t}{\omega_{LO}+\omega_{RF}}$, while for antenna element 2 and antenna element 3 is $(t_6 - t_4) + \frac{2\omega_{LO}\Delta t}{\omega_{LO}+\omega_{RF}}$. Thus, the time difference remains constant for each neighbouring antenna element of each TAA of Figure 3.

Hence, we have shown mathematically that our beamforming signal generation is capable of maintaining a constant time-delay difference between the neighbouring photo-detected mmwave frequencies fed into different antenna elements. Thus, our all-optical design is capable of supporting beamforming, while simultaneously implementing mmWave upconversion.

## D. BEAMFORMING SIMULATION RESULTS

In our system, a 30 mm CFBG is used for introducing the delay required at the different wavelengths in order to support beamsteering. The time-delay imposed on the different wavelengths when the total chirp of the grating period of CFBG is set to 1.05 nm, which represents the difference between first period and the last period in the CFBG. Our simulations were carried out by using the OPTGRATING software and the delay vs wavelength and frequency is shown in Figure 6, where the wavelength range spans from 1549 nm to 1551 nm.

Thus, the spectral width, which is refered to as the spectral range of reflected wavelength and changes with the total chirp [35], determines the time-delay difference as a function of frequency spacing. Proposed by [35], the total spectral width as well as total chirp can be adjusted by tuning a supported beam's deflection, resulting in a linear time-delay difference vs spectral width.
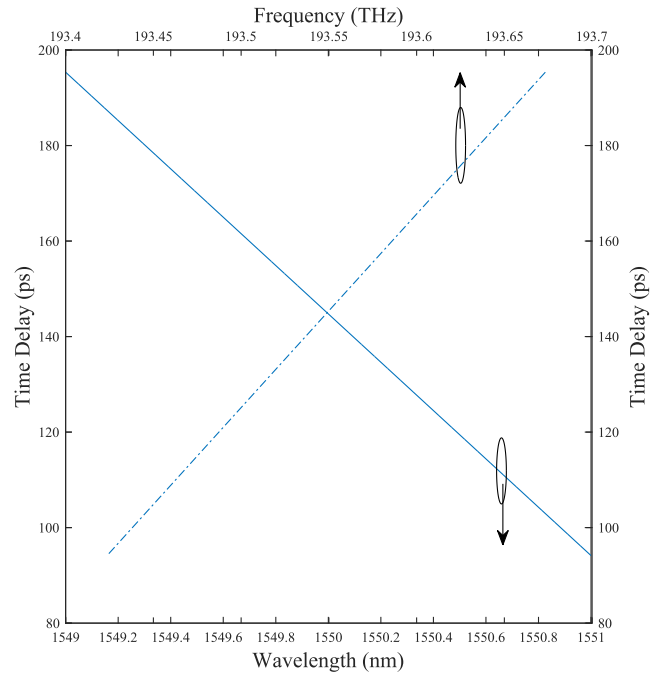
**FIGURE 6.** Linear time delay vs wavelength and frequency of CFBG with the total chirp of 1.05 nm.
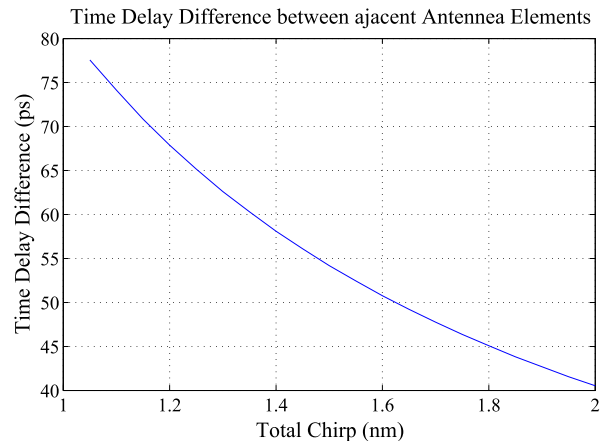
**FIGURE 7.** Total chirp vs time delay difference.

Furthermore, as analysed in Section II-C, the CFBG facilitates a constant time-delay difference of $(t_4 - t_2) + \frac{2\omega_{LO}\Delta t}{\omega_{LO}+\omega_{RF}}$, where $\Delta t$ is the time-delay difference for a 28 GHz spacing and a time-delay difference $t_4 - t_2$ at a 50 GHz spacing. Thus, according to the linear relationship seen in Figure 6 and 7, the time-delay difference between the adjacent antenna elements is 77.6 ps, when a total chirp of 1.05 nm is applied. Then, by changing the total chirp of the tunable CFBG of Figure 3, we obtain the corresponding relationship between the total chirp and the time-delay difference regarding our design as shown in Figure 7, where the time-delay difference range spans from 77.6 ps to 40.6 ps, when increasing the total chirp from 1.05 nm to 2.05 nm with a step-size of 0.05 nm. Then, according to the time-delay difference
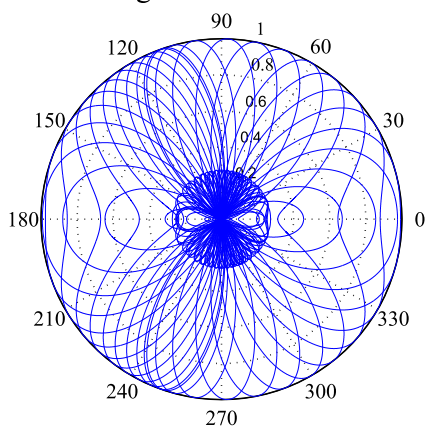
Beamforming with N=4 antenna arrays



**FIGURE 8.** Beamforming pattern.

| Parameter | Value |
|---|---|
| Bit rate | 2 Gbps (2-antenna SM) 3 Gbps (4-antenna SM) |
| RF signal | 3 GHz |
| LD Center Wavelength | 1550 nm |
| LD Power | 1 mW |
| Drive Frequency (MZM) | 25 GHz |
| Achieved mmWave frequency | 28 GHz |
| MZM mode | push-pull mode |
| Fiber type | DSF |
| Fiber length | 10 km |
| Channel Model | Split-Step Fourier Method |
| Modulation Type | BPSK |
| Wireless Channel | Rayleigh Fading Channel |
| Wireless Detection | ML Detection |
| Beamforming Type | 4 Antenna Elements |
| Simulation Environment | MATLAB |

range, we obtain a beam coverage range of almost 360°, as shown in Figure 8.

### E. SYSTEM SIMULATION RESULTS AND DISCUSSIONS
In this section we analyse the performance of our SM system employing A-RoF combined with all-optical beamforming and up-conversion to mmWave frequency. We compare our proposed system to the conventional SM system operating without A-RoF in the context of a single-RRH for verifying our centralized design philosophy, which only imposes an almost negligible performance degradation. However, before discussing the results, let us first consider the MIMO channel model after the fiber transmission and study its effect on the system's performance.

In conventional MIMO systems employing $N_t$ transmit antennas and $N_r$ receive antennas, we model the received signal using $\mathbf{Y} = \mathbf{HX} + \mathbf{n}$, where $\mathbf{Y}$ represents the received symbol vector of size $(N_r \times 1)$, $\mathbf{H}$ is the MIMO channel matrix of size $(N_r \times N_t)$, $\mathbf{X}$ denotes the transmitted symbol vector of size $(N_t \times 1)$ and $\mathbf{n}$ is a $(N_r \times 1)$-element Additive White Gaussian Noise (AWGN) vector. However, during its fiber-based transition, the symbol vector $\mathbf{X}$ is affected by the fiber impairments, such as fiber attenuation, chromatic dispersion and fiber non-linearity in addition to the noise imposed by photo-detection [29]. Hence, in our system we model the SM based MIMO transmission after fiber-based transmission as follows:

$$\mathbf{Y} = \mathbf{H}\alpha\mathbf{X} + \mathbf{n}, \qquad (9)$$

where $\alpha$ includes the effect of the fiber impairments and optical noise, while $\mathbf{n}$ includes the effect of the AWGN imposed by the RF circuits. Note that the channel state information now includes the wireless channel fading as well as the fiber impairments and these are jointly estimated at the receiver. In other words, the receiver will estimate $\mathbf{H}\alpha$.

Furthermore, in the proposed system, the beamsteering direction has to be known at the transmitter and this problem has been widely discussed in the literature, where several

accurate Angle of Departure (AoD) estimation techniques have been proposed [36], [37]. Based on the above-mentioned design, we simulated our A-RoF network and compared the Bit Error Ratio (BER) of the received signal to that of its equivalent electronic SM counterpart dispensing with A-RoF transmission. Table 1 summarizes the parameters used in our system. The bit rate given is the joint bit rate of implicit bits and classic modulated bits, where, for example, a classic modulated BPSK scheme of 1 Gbps can achieve a joint bit rate of 2 Gbps for two-antenna SM and 3 Gbps for four-antenna SM. The MS-STSK scheme applies the bit rate similarly, which is detailed in [38].

An RF signal having a 3 GHz carrier is directly modulated by the LDs of Figure 3, while a drive frequency of 25 GHz is used by the MZM. This allows up-converting the 3 GHz signal to a mmWave signal of 28 GHz. The resultant frequency depends on the specific combination of the RF and the drive frequency of the MZM. Owing to the utilization of the DSF, where the zero-dispersion wavelength is in the vicinity of 1550 nm, the proposed design is capable of mitigating the fiber dispersion hence achieving an improved beamforming performance. We employed 4 elements per TAA for the sake of showing the benefits of beamforming.

In order to show that our proposed A-RoF system has a minimal impact on the BER performance compared to that of the conventional SM system, we transmit our mmWave signal over the wireless channel and then compare the performance of the two systems. The beamformed mmWave SM signal obtained after A-RoF transmission is impaired by the mmWave wireless channel [15]. Figure 9 shows the BER performance of $(N_t \times N_r)=(2 \times 1)$, $(2 \times 2)$, $(4 \times 1)$, $(4 \times 2)$ and $(4 \times 4)$ MIMO systems operating both with and without A-RoF, while analogue beamforming is employed at the transmitter and receiver. Again, four-element TAAs are employed for attaining beamforming in our simulated system.
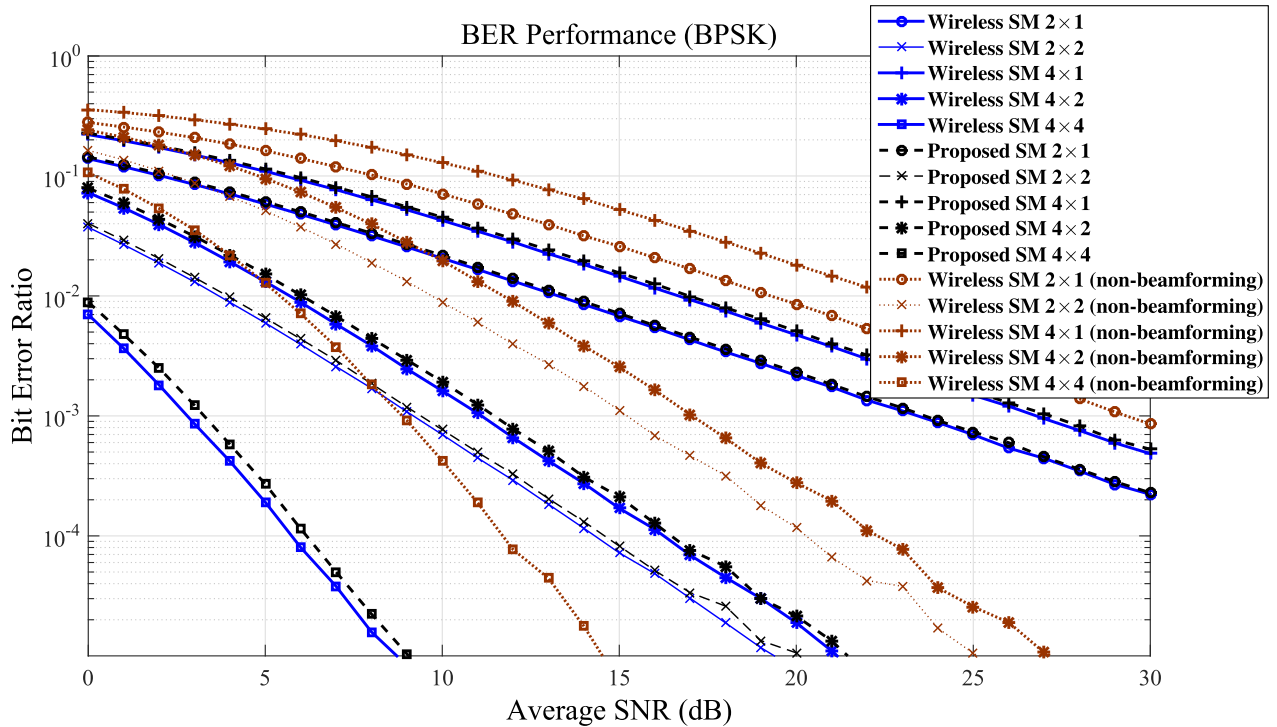
**FIGURE 9.** The BER performance of our SM scheme compared to that of the conventional electronic SM scheme using the parameters summarized in Table 1.

In the conventional electronic SM encoding scheme of Section II-A, the antenna selection is based on implicitly conveyed symbols. In our proposed system, we modulate the implicit symbol and the classically modulated symbol onto each side-band of the ODSB signal generated by the LDs of Figure 3.

Furthermore, we applied the implicit bits to a $2^L$-PSK/QAM modulation scheme, where $2^L$ also represents the number of antenna elements, while the classic modulated bits on Binary Phase-Shift Keying (BPSK) format. Then, before feeding the antennas, the corresponding $2^L$-PSK/QAM symbols are recovered and then the implicit bits will select the activated antenna transmitting the up-converted mmWave signals carrying the modulated BPSK symbols. Thus, the implicit bits of the 2-antenna SM scheme are carried in the left side-band of Figure 3 as a BPSK symbol, while for the 4-antenna case, they are modulated as QPSK. The bit rate of the classic BPSK modulated bits is 1 Gbps, while the BPSK implicit bits convey a bit rate of 1 Gbps, and the QPSK implicit bits support a bit rate of 2 Gbps, hence achieving a multiplexed bits rate of 2 Gbps for our 2-antenna SM and 3 Gbps for 4-antenna SM.

As shown in Figure 9, when no optical amplifier is used, the BER performance of our proposed system shows a slight degradation, which is caused by the fiber's attenuation, non-linearity and optical noise. This degradation can be readily mitigated by introducing an optical amplifier, as shown in the next section in the context of MS-STSK. Moreover, in Figure 9, the BER performance of wireless systems

dispensing with beamforming is shown, where a 6 dB SNR gain is achieved by beamforming using $N = 4$ antenna arrays.

As observed in Figure 9, by employing lower-complexity remote radio heads, our proposed SM scheme shows a slight BER degradation in comparison to the conventional SM scheme. In the following scheme, we incorporate MS-STSK into our system, which is a generalized architecture subsuming both SM and STSK.

## III. A-RoF NETWORK DESIGN FOR MS-STSK
In this section, the MS-STSK scheme is intrinsically amalgamated with our A-RoF downlink combined with all-optical beamforming and upconversion to a mmWave frequency for transmission over the mmWave wireless channel.

### A. CONVENTIONAL MS-STSK SCHEME
MS-STSK was proposed in [27] as a generalization of SM and STSK, where the data bit sequence is partitioned into three streams that convey the antenna selection, the dispersion matrix selection and the PSK/QAM modulated symbol. As shown in Figure 10, the data stream is divided into three parts: the bit stream $B_1$ is used for antenna selection, while the bit streams $B_2$ and $B_3$ are used for STSK encoding. In STSK encoding, $B_2 = log_2Q$ bits are used for selecting one out of $Q$ dispersion matrices, while $B_3$ is represented by the PSK/QAM symbol. The output of the STSK encoder is transmitted using $N_{RF}$ RF chains, which are switched to a specific combination of $N_{RF}$ out of the $N_t$ antennas with the aid of the
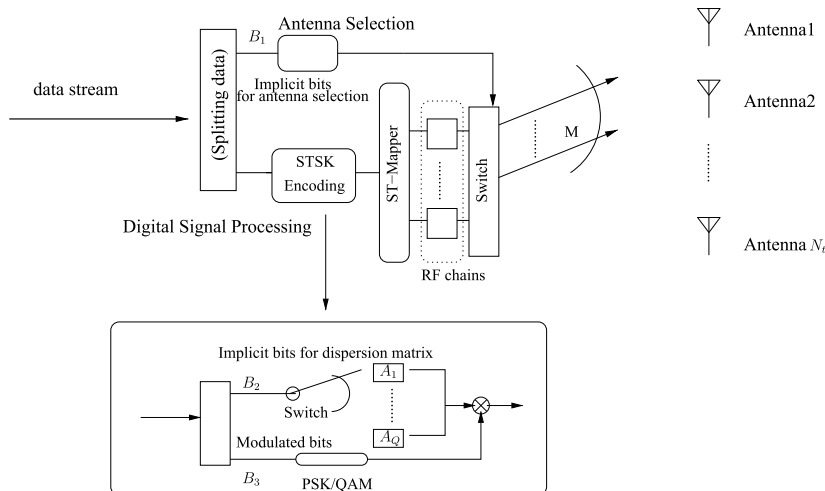
**FIGURE 10.** Conventional electronic MS-STSK encoding scheme employed at the Base Stations of the conventional cellular architecture.

antenna selection unit. Hence, the $B_1$ and $B_2$ bit streams of Figure 10 are implicitly conveyed over the activated Antenna Combination (AC) index and the dispersion matrix selected, respectively.

The MS-STSK scheme is capable of utilising a compelling diversity and multiplexing trade-off [27]. As mentioned above, MS-STSK can be introduced into our system by imposing a slight extra complexity on the remote radio head compared to the A-RoF-aided SM design of Figure 3. In this section, we denote the MS-STSK system as MS-STSK $(N_t, M, N_r, T, Q, \mathcal{L} - PSK/QAM)$, where each symbol is characterized in Table 2. In the following section, we will discuss our A-RoF-aided MS-STSK design.

**TABLE 2.** MS-STSK symbol notations.

| Parameter | Representation |
|-----------|----------------|
| $N_t$ | Transmitter Antenna |
| $M$ | STSK Space dimension |
| $Nr$ | Receive antenna |
| $Q$ | Number of dispersion matrix |
| $T$ | STSK Time Slots |
| $\mathcal{L}$ | PSK/QAM constellation size |

### B. PROPOSED A-RoF-AIDED MS-STSK DESIGN
The MS-STSK design is further extended and improved from the SM design proposed in Section II, as shown in Figure 11. Three changes have been made in the A-RoF aided MS-STSK system compared to the SM counterpart of Figure 3.

1) The $x_1$ implicit symbols carry the bits $B_1$ and $B_2$ of both the selected AC and of the dispersion matrix, rather than only of the antenna selection information of SM, which is mapped to the left-side band of the ODSB signals generated before the MZM of Figure 11. Here, the $B_1$ and $B_2$ bits are concatenated and then mapped to $x_1$.

2) If the number of implicit bits containing $B_1$ and $B_2$ is $L_{MS}$, then the symbols carrying the implicit bits would be mapped to $2^{L_{MS}} - PSK/QAM$ alphabet. Thus, the implicit bits convey both the information for antenna selection and the dispersion matrix selection. Hence, more implicit bits are conveyed by MS-STSK and therefore a larger constellation size is required to transmit the implicit bits of MS-STSK over the optical fiber, which is more susceptible to both fiber impairments and to optical noise. We invoked an Erbium-doped fiber amplifier (EDFA) before the OIL of Figure 11 in order to mitigate these effects by improving the optical SNR.

3) Furthermore, in the remote radio head of Figure 11, the recovered implicit bits are split into the $B_1$ and $B_2$ streams, which represent the antenna selection bits and the dispersion matrix selection bits, respectively. Then, the classic modulated symbol carried by the up-converted mmWave signal is multiplied by the dispersion matrix selected and then transmitted over the AC selected, while beamforming is introduced by CFBG, which was discussed in Section II.

Our A-RoF-aided MT-STSK scheme constitutes an extension of the A-RoF-aided SM scheme discussed in Section II. As shown in Figure 11, the ODSB modulated by $x_1$ and $x_2$ is up-converted to a mmWave frequency, and an optically aided beamforming scheme based on the CFBG philosophy of [35] is created. Thus, we adjusted the A-RoF network conceived for SM to include MS-STSK by adding a few extra components, such as an EDFA and the dispersion matrix selection scheme of Figure 11. Next, we present our simulation results and related discussion to verify our system.

### C. SYSTEM SIMULATION RESULTS AND DISCUSSIONS
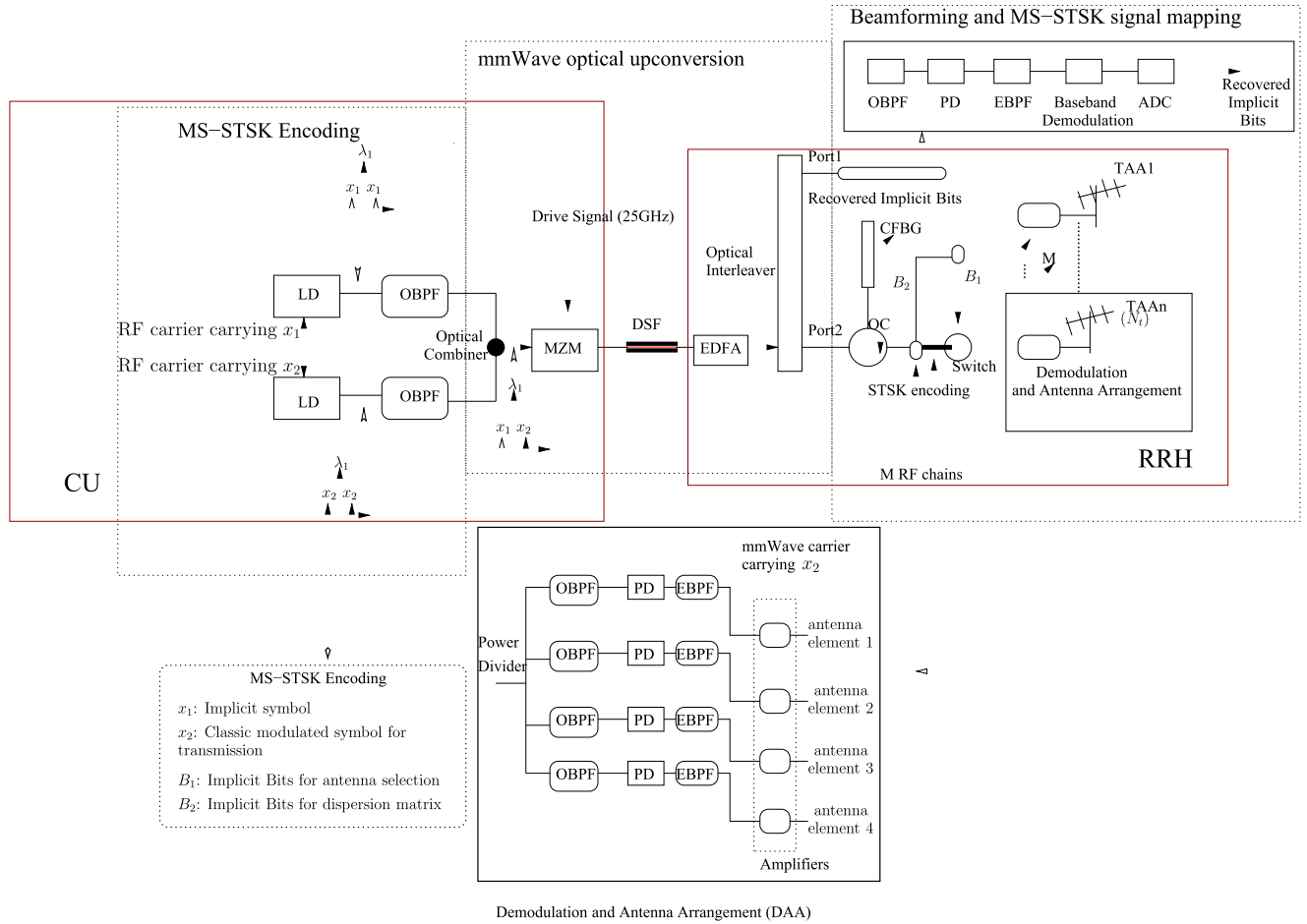Let us now consider an MS-STSK (4, 2, 2, 2, 4, BPSK) system based on the design depicted in Figure 11.

**FIGURE 11.** A centralized A-RoF aided MS-STSK Network. The CU implements digital modulation, carrier modulation, E-O conversion and MS-STSK encoding, while the RRH carries out the radio functions (filtering, O-E conversion, photo-detection and amplifying radio transmission), as well as MS-STSK implicit data recovery and MS-STSK switching.

**TABLE 3.** Simulation parameters.

| Parameter | Value |
|---|---|
| Bit rate | 5 Gbps (BPSK system) 10 Gbps (16-QAM system) |
| RF signal | 3 GHz |
| LD Center Wavelength | 1550 nm |
| LD Power | 0.1 mW |
| Drive Frequency (MZM) | 25 GHz |
| Achieved mmWave frequency | 28 GHz |
| MZM mode | push-pull mode |
| Fiber type | DSF |
| Fiber length | 10 km |
| Channel Model | Split-Step Fourier Method |
| Modulation Type | BPSK/16QAM |
| EDFA Gain | 20 dB |
| Wireless Channel | Rayleigh Fading Channel |
| Wireless Detection | ML Detection |
| Beamforming Type | 4 Antenna Elements |
| Simulation Environment | MATLAB |

The simulation parameters are shown in Table 3. Due to the larger number of implicit bits of MS-STSK than that of our SM scheme, a higher order modulation scheme such as

16-QAM is required, which is more susceptible to fiber non-linearity. The LD power is reduced to 0.1 milliWatt (mW) for the sake of mitigating the effect of non-linearity induced-phase shifts.

Before being mapped to the two side-bands of the ODSB scheme shown in Figure 11, the implicit bits used for the MS-STSK scheme of Figure 11 are mapped to the 16-QAM symbols $x_1$, where two bits are used for selection of a dispersion matrix and the other two bits are used for the antenna selection. Finally, the classic modulated symbols $x_2$ are BPSK symbols. Using the same data set for the dispersion matrix as in [27], Figure 12 shows the BER performance of conventional electronic MS-STSK both with and without beamforming using $N = 4$ antenna arrays and of our proposed A-RoF-aided MS-STSK system. The comparisons are based on $(4 \times 4)$, $(4 \times 2)$ and $(4 \times 1)$ MIMO schemes, where analogue beamforming using four antenna-elements is employed. It is clearly observed that there is only a minor BER degradation, when our fiber network is invoked. Moreover, recall from Figure 9, that without EDFA, there is still a modest degradation in BER performance. However, owing to the requirement of using a higher-order fiber-modulation for MS-STSK,
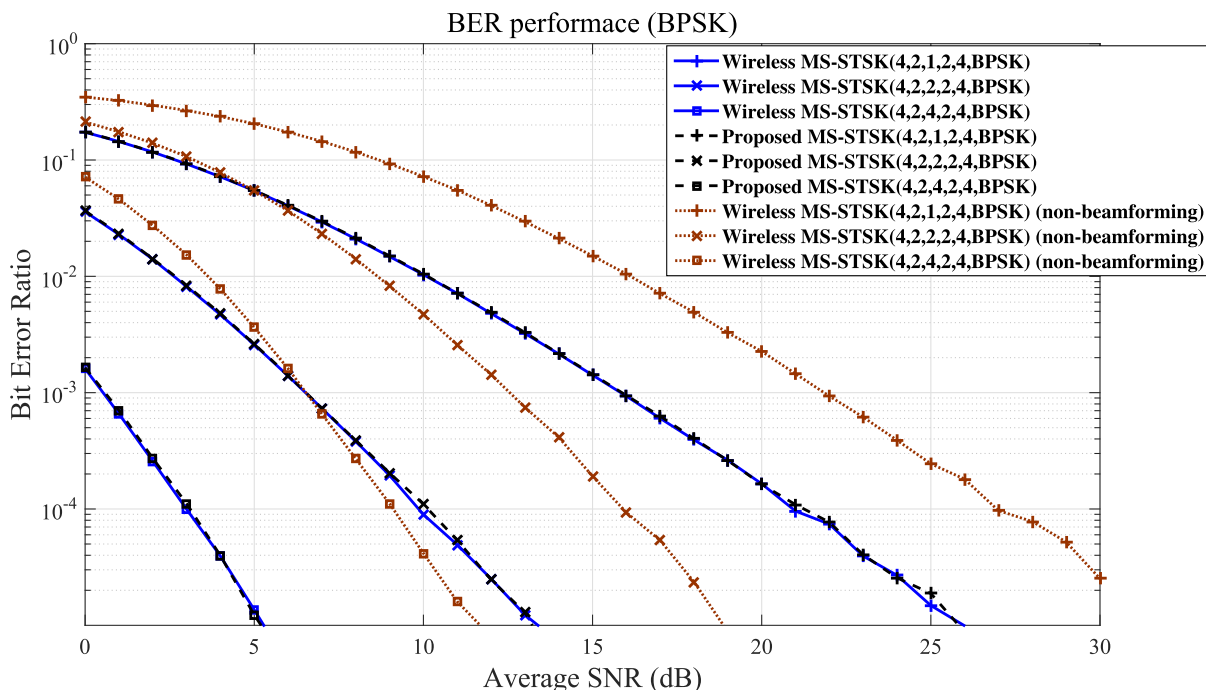
**FIGURE 12.** BER performance of conventional electronic MS-STSK and of our proposed MS-STSK scheme for 5Gbps BPSK modulated signal using the parameters summarised in Table 3.
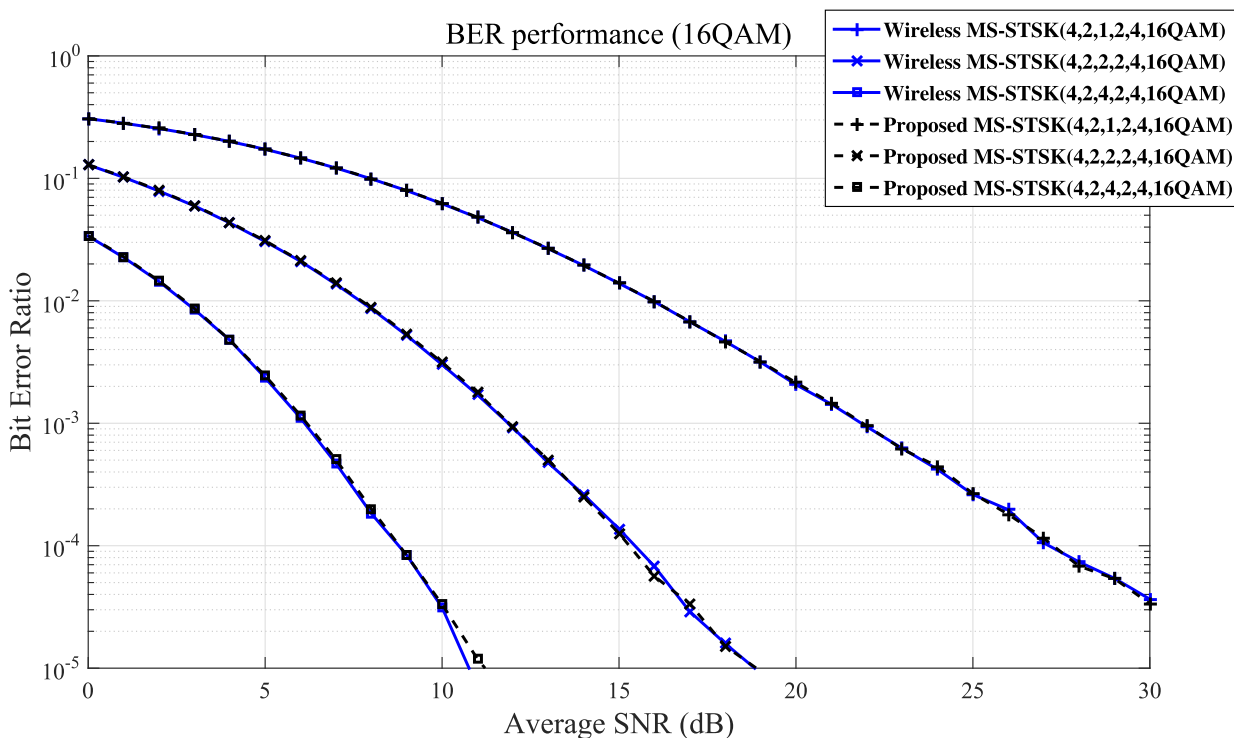


**FIGURE 13.** BER performance of conventional electronic MS-STSK and of our proposed MS-STSK scheme for 10Gbps 16 QAM using the parameters summarised in Table 3.

which is more susceptible to fiber impairments, the proposed MT-STSK system relies on an EDFA having a 20 dB gain in order to compensate for the degradation. Additionally, observe in Figure 12 that the beamforming aided system has a 6 dB beamforming gain.

Furthermore, to verify that our system is scalable and suitable for high data rates, we mapped the classic modulated bits to a 16 QAMs while invoking another 16-QAM scheme for the implicit bits, transmitting a 10 Gbps signal using the same MT-STSK scheme as above. As discussed above, 16 QAM is

more susceptible than BPSK to the fiber impairment, hence an EDFA of 26 dB gain is invoked. Figure 13 shows our comparison of the $(4 \times 4)$, $(4 \times 2)$ and $(4 \times 1)$ MS-MTSK MIMO schemes. Given that only a modest degradation is observed, we conclude that our SM/MS-STSK A-RoF network benefits from all-optical processing, whilst avoiding the ADC-and-DAC-related complexity in the remote radio head of Figure 11.

MT-STSK is a general scheme subsuming both SM and STSK, where space-time coding can be included, leading increased flexibility to our proposed system. Additionally, the beamforming solely relies on CFBG and the corresponding wavelengths, as discussed in Section II.

## IV. CONCLUSIONS

In this paper, we presented a A-RoF aided SM/MS-STSK downlink network, where SM and MS-STSK are implemented in a centralized processing fashion. This design is capable of substantially reducing the complexity of the remote radio head, when intrinsically amalgamated with SM or MS-STSK. Our SM/MS-STSK design is capable of achieving optical up-conversion to mmWave carriers, whilst supporting optical fiber aided beamforming. Additionally, we achieved a bit rate of 10 Gbps for 16QAM and 10 km DSF in our MS-STSK fiber based A-RoF network, where the BER performance shows little degradation compared to those without fiber networks.

## REFERENCES

[1] L. Hanzo, M. El-Hajjar, and O. Alamri, "Near-capacity wireless transceivers and cooperative communications in the MIMO era: Evolution of standards, waveform design, and future perspectives," *Proc. IEEE*, vol. 99, no. 8, pp. 1343–1385, Aug. 2011.

[2] A. Goldsmith, *Wireless Communications*. Cambridge, U.K.: Cambridge Univ. Press, 2005.

[3] L. Hanzo, H. Haas, S. Imre, D. O'Brien, M. Rupp, and L. Gyongyosi, "Wireless myths, realities, and futures: From 3G/4G to optical and quantum wireless," *Proc. IEEE*, vol. 100, pp. 1853–1888, May 2012.

[4] S. Rangan, T. S. Rappaport, and E. Erkip, "Millimeter-wave cellular wireless networks: Potentials and challenges," *Proc. IEEE*, vol. 102, no. 3, pp. 366–385, Mar. 2014.

[5] V. A. Thomas, M. El-Hajjar, and L. Hanzo, "Performance improvement and cost reduction techniques for radio over fiber communications," *IEEE Commun. Surveys Tuts.*, vol. 17, no. 2, pp. 627–670, 2nd Quart., 2015.

[6] J. M. B. Oliveira, H. M. Salgado, and M. R. D. Rodrigues, "A new mse channel estimator optimized for nonlinearly distorted faded OFDM signals with applications to radio over fiber," *IEEE Trans. Commun.*, vol. 62, no. 8, pp. 2977–2985, Aug. 2014.

[7] D. Novak *et al.*, "Radio-over-fiber technologies for emerging wireless systems," *IEEE J. Quantum Electron.*, vol. 52, no. 1, Jan. 2016, Art. no. 0600311.

[8] S. Z. Pinter and X. N. Fernando, "Estimation and equalization of fiber-wireless uplink for multiuser CDMA 4G networks," *IEEE Trans. Commun.*, vol. 58, no. 6, pp. 1803–1813, Jun. 2010.

[9] A. Checko *et al.*, "Cloud RAN for mobile networks—A technology overview," *IEEE Commun. Surveys Tuts.*, vol. 17, no. 1, pp. 405–426, 1st Quart., 2015.

[10] M. Peng, K. Zhang, J. Jiang, J. Wang, and W. Wang, "Energy-efficient resource assignment and power allocation in heterogeneous cloud radio access networks," *IEEE Trans. Veh. Technol.*, vol. 64, no. 11, pp. 5275–5287, Nov. 2015.

[11] V. N. Ha, L. B. Le, and N. D. Đào, "Coordinated multipoint transmission design for cloud-RANs with limited fronthaul capacity constraints," *IEEE Trans. Veh. Technol.*, vol. 65, no. 9, pp. 7432–7447, Sep. 2016.

[12] M. Peng, C. Wang, V. Lau, and H. V. Poor, "Fronthaul-constrained cloud radio access networks: Insights and challenges," *IEEE Wireless Commun.*, vol. 22, no. 2, pp. 152–160, Apr. 2015.

[13] Y. Li, M. El-Hajjar, and L. Hanzo, "Joint space-time block-coding and beamforming for the multiuser radio over plastic fiber downlink," *IEEE Trans. Veh. Technol.*, vol. 67, no. 3, pp. 2781–2786, Mar. 2017.

[14] G. S. D. Gordon, M. J. Crisp, R. V. Penty, and I. H. White, "Experimental evaluation of layout designs for $3 \times 3$ MIMO-enabled radio-over-fiber distributed antenna systems," *IEEE Trans. Veh. Technol.*, vol. 63, no. 2, pp. 643–653, Feb. 2014.

[15] T. S. Rappaport *et al.*, "Millimeter wave mobile communications for 5G cellular: It will work!" *IEEE Access*, vol. 1, pp. 335–349, May 2013.

[16] V. A. Thomas, M. El-Hajjar, and L. Hanzo, "Millimeter-wave radio over fiber optical upconversion techniques relying on link nonlinearity," *IEEE Commun. Surveys Tuts.*, vol. 18, no. 1, pp. 29–53, 1st Quart., 2016.

[17] Y. Xiang, C. Chen, C. Zhang, and K. Qiu, "Wired/wireless access integrated RoF-PON with scalable generation of multi-frequency MMWs enabled by polarization multiplexed FWM in SOA," *Opt. Exp.*, vol. 21, no. 1, pp. 1218–1225, 2013.

[18] C. Zhang, L. Wang, and K. Qiu, "Proposal for all-optical generation of multiple-frequency millimeter-wave signals for RoF system with multiple base stations using FWM in SOA," *Opt. Exp.*, vol. 19, no. 15, pp. 13957–13962, 2011.

[19] Y. Xiang, N. Jiang, C. Chen, C. Zhang, and K. Qiu, "Wired/wireless access integrated RoF-PON with scalable generation of multi-frequency MMWs enabled by tunable optical frequency comb," *Opt. Exp.*, vol. 21, no. 17, pp. 19762–19767, 2013.

[20] C. Zhang, C. Chen, and K. Qiu, "Hybrid bidirectional radio-over-fiber-based orthogonal frequency division multiple access-passive optical network supporting 60/120 GHz using offset quadrate phase shift keying," *Opt. Eng.*, vol. 54, no. 9, p. 096108, 2015.

[21] Z. Cao *et al.*, "Advanced integration techniques on broadband millimeter-wave beam steering for 5G wireless networks and beyond," *IEEE J. Quantum Electron.*, vol. 52, no. 1, Jan. 2016, Art. no. 0600620.

[22] M. Di Renzo, H. Haas, A. Ghrayeb, S. Sugiura, and L. Hanzo, "Spatial modulation for generalized MIMO: Challenges, opportunities, and implementation," *Proc. IEEE*, vol. 102, no. 1, pp. 56–103, Jan. 2014.

[23] R. Y. Mesleh, H. Haas, S. Sinanovic, C. W. Ahn, and S. Yun, "Spatial modulation," *IEEE Trans. Veh. Technol.*, vol. 57, no. 4, pp. 2228–2241, Jul. 2008.

[24] C.-X. Wang *et al.*, "Cellular architecture and key technologies for 5G wireless communication networks," *IEEE Commun. Mag.*, vol. 52, no. 2, pp. 122–130, Feb. 2014.

[25] S. Sugiura, S. Chen, and L. Hanzo, "A universal space-time architecture for multiple-antenna aided systems," *IEEE Commun. Surveys Tuts.*, vol. 14, pp. 401–420, 2nd Quart., 2012.

[26] S. Sugiura, S. Chen, and L. Hanzo, "Coherent and differential space-time shift keying: A dispersion matrix approach," *IEEE Trans. Commun.*, vol. 58, no. 11, pp. 3219–3230, Nov. 2010.

[27] I. A. Hemadeh, M. El-Hajjar, S. Won, and L. Hanzo, "Multi-set space-time shift-keying with reduced detection complexity," *IEEE Access*, vol. 4, pp. 4234–4246, 2016.

[28] T. Erdogan, "Fiber grating spectra," *J. Lightw. Technol.*, vol. 15, no. 8, pp. 1277–1294, Aug. 1997.

[29] G. P. Agrawal, *Fiber-Optic Communication Systems*, vol. 222. Hoboken, NJ, USA: Wiley, 2012.

[30] H. Chettat, L. M. Simohamed, Y. Bouslimani, and H. Hamam, "RoF networks: A comprehensive study," in *Proc. 3rd Int. Symp. Wireless Pervasive Comput.*, May 2008, pp. 495–498.

[31] M. El-Hajjar and L. Hanzo, "Multifunctional MIMO systems: A combined diversity and multiplexing design perspective," *IEEE Wireless Commun.*, vol. 17, no 2, pp. 73–79, Apr. 2010.

[32] S. Ghafoor and L. Hanzo, "Reduced dispersion duplex DQPSK radio-over-fiber communications using single-laser-based multiple side-bands," in *Proc. IEEE Int. Conf. Commun. (ICC)*, Jun. 2011, pp. 1–5.

[33] J. L. Corral, J. Marti, S. Regidor, J. M. Foster, R. Laming, and M. J. Cole, "Continuously variable true time-delay optical feeder for phased-array antenna employing chirped fiber grating," *IEEE Trans. Microw. Theory Techn.*, vol. 45, no. 8, pp. 1531–1536, Aug. 1997.

[34] J. Yao, J. Yang, and Y. Liu, "Continuous true-time-delay beamforming employing a multiwavelength tunable fiber laser source," *IEEE Photon. Technol. Lett.*, vol. 14, no. 5, pp. 687–689, May 2002.

[35] Y. Liu, J. Yang, and J. Yao, "Continuous true-time-delay beamforming for phased array antenna using a tunable chirped fiber grating delay line," *IEEE Photon. Technol. Lett.*, vol. 14, no. 8, pp. 1172–1174, Aug. 2002.

[36] A. Alkhateeb, O. El Ayach, G. Leus, and R. W. Heath, Jr., "Channel estimation and hybrid precoding for millimeter wave cellular systems," *IEEE J. Sel. Topics Signal Process.*, vol. 8, no. 5, pp. 831–846, Oct. 2014.

[37] C. Zhang, D. Guo, and P. Fan, "Tracking angles of departure and arrival in a mobile millimeter wave channel," in *Proc. IEEE ICC*, May 2016, pp. 1–6.

[38] I. A. Hemadeh, M. El-Hajjar, and L. Hanzo, "Hierarchical multi-functional layered spatial modulation," *IEEE Access*, vol. 6, pp. 9492–9533, 2018.

**MOHAMMED EL-HAJJAR** received the Ph.D. degree in wireless communications from the University of Southampton, U.K., in 2008. He joined Imagination Technologies as a Design Engineer, where he was involved in designing and developing Imagination's multi-standard communications platform, which resulted in three patents. He is currently an Associate Professor with the Department of Electronics and Computer Science, University of Southampton. He has published a Wiley - IEEE book and in excess of 80 journal and conference papers. His research interests include the development of intelligent communications systems, energy-efficient transceiver design, MIMO, millimeter-wave communications, and radio-over-fiber network design. He is the recipient of several academic awards.

**YICHUAN LI** received the B.Sc. degree in optics information science and technology from the China University of Petroleum (East China), Qingdao, China, in 2012, and the M.Sc. degree in wireless communications from the University of Southampton, Southampton, U.K., in 2014, where he is currently pursuing the Ph.D. degree. In 2017, he was a Research Assistant with the Lightwave Communications Laboratory, The Chinese University of Hong Kong. His research is focused on the radio over fiber for backhaul, front-haul, and indoor communication network. His research interests include millimeter-wave over fiber, optical fiber-aided analogue beamforming techniques, multifunctional MIMO, and mode division multiplexing in multimode fiber (both glass multimode fiber and plastic optical fiber).

**LAJOS HANZO** (F'04) received the D.Sc. degree in electronics in 1976 and the Ph.D. in 1983. During his 40-year career in telecommunications, he has held various research and academic posts in Hungary, Germany, and U.K. Since 1986, he has been with the School of Electronics and Computer Science, University of Southampton, U.K. He is currently directing a 60-strong academic research team, working on a range of research projects in the field of wireless multimedia communications sponsored by industry, the Engineering and Physical Sciences Research Council, U.K., the European Research Council's Advanced Fellow Grant, and the Royal Society's Wolfson Research Merit Award. He is an enthusiastic supporter of industrial and academic liaison and he offers a range of industrial courses. He has successfully supervised 111 Ph.D. students, co-authored 18 John Wiley/IEEE Press books on mobile radio communications totalling in excess of 10 000 pages, published over 1700 research contributions at the IEEE Xplore. He has over 30 000 citations. He was a FREng, FIET, and Fellow of EURASIP. He received an Honorary Doctorate from the Technical University of Budapest in 2009 and The University of Edinburgh in 2015. In 2016, he was admitted to the Hungarian Academy of Science. He is a Governor of the IEEE VTS. He served as the TPC Chair and the General Chair of the IEEE conferences, presented keynote lectures and has been awarded a number of distinctions. He is the Chair in telecommunications with the University of Southampton. From 2008 to 2012, he was an Editor-in-Chief of the IEEE Press and a Chaired Professor at Tsinghua University, Beijing.

**IBRAHIM A. HEMADEH** received the B.Eng. degree (Hons.) in computer and communications engineering from the Islamic University of Lebanon, Lebanon, in 2010, and the M.Sc. degree (Hons.) in wireless communications and the Ph.D. degree in electronics and electrical engineering from the University of Southampton, U.K., in 2012 and 2017, respectively. He is currently a Post-Doctocal Researcher at Southampton Wireless Group, University of Southampton. His research interests mainly include millimeter-wave communications, multi-functional MIMO, multi-dimensional (time, space, and frequency) transceiver designs, channel coding, and also multi-user MIMO.

・・・